JOURNAL OF GEOPHYSICAL RESEARCH: SPACE PHYSICS, VOL. 118, 5891–5905, doi:10.1002/jgra.50487, 2013

A theory of ionospheric response to upward-propagating tides: Electrodynamic effects and tidal mixing effects

Yosuke Yamazaki[1] and Arthur D. Richmond[1]

Received 11 March 2013; revised 14 June 2013; accepted 30 July 2013; published 10 September 2013.

[1] The atmospheric tide at ionospheric heights is composed of those locally generated and those propagated from below. The role of the latter in producing the variability of the daytime ionosphere is examined using the National Center for Atmospheric Research Thermosphere-Ionosphere-Electrodynamics General Circulation Model. The impact of upward-propagating tides is evaluated by running simulations with and without tidal forcing at the lower boundary (approximately 96 km), which imitates the effect of tides from below. When migrating diurnal and semidiurnal tides at the lower boundary is switched on, the intensity of *E* region currents and the upward velocity of the equatorial *F* region vertical plasma drift rapidly increase. The low-latitude ionospheric total electron content (TEC) first increases, then gradually decreases to below the initial level. The initial increase in the low-latitude TEC is caused by an enhanced equatorial plasma fountain while the subsequent decrease is due to changes in the neutral composition, which are characterized by a global-scale reduction in the mass mixing ratio of atomic oxygen O_1. The results of further numerical experiments indicate that the mean meridional circulation induced by dissipating tides in the lower thermosphere is mainly responsible for the O_1 reduction; it acts like an additional turbulent eddy and produces a "mixing effect" that enhances net downward transport and loss of O_1. It is stressed that both electrodynamic effects and mixing effects of upward-propagating tides can be important in producing the variability of ionospheric plasma density. Since the two mechanisms act in different ways on different time scales, the response of the actual ionosphere to highly variable upward-propagating tides is expected to be complex.

Citation: Yamazaki, Y., and A. D. Richmond (2013), A theory of ionospheric response to upward-propagating tides: Electrodynamic effects and tidal mixing effects, *J. Geophys. Res. Space Physics*, *118*, 5891–5905, doi:10.1002/jgra.50487.

1. Introduction

[2] Atmospheric tides are global-scale oscillations of atmospheric quantities (such as pressure, temperature, and winds) with periods of harmonics of a solar or lunar day [*Lindzen and Chapman*, 1969]. Solar tides are predominantly of thermal (not gravitational) origin, excited through periodic absorption of solar radiation by H_2O in the troposphere, by O_3 in the stratosphere, and by O_1, O_2, and N_2 in the thermosphere above 100 km. (Note that in this paper, we use O_1 instead of O to denote atomic oxygen.) Meanwhile, minor lunar tides are almost entirely of gravitational origin. Some tides have upward-propagating properties. They get larger in amplitude as the waves travel upward from the source region. This is because the waves tend to conserve energy per unit volume ($\frac{1}{2}\rho A^2$, where ρ is density and A is velocity amplitude), propagating through the atmosphere where the background density decreases with height. In the lower atmosphere, tidal wind amplitudes are small compared to the background wind speed, but they grow with height and reach their maximum of many tens of meters per second in the mesosphere and lower thermosphere (MLT) region (between about 90 and 140 km), where damping of tidal waves occurs due to eddy and molecular dissipation. Atmospheric tides are highly variable in the MLT region. It is not uncommon to observe that tidal amplitudes increase or decrease by a factor of 2–3 within a week [*Forbes*, 1984, and references therein]. The tidal variability in the MLT region probably reflects the variable state of the atmosphere below. For example, planetary waves in the lower and middle atmosphere can lead to short-term tidal variability in the MLT region by nonlinearly interacting with tides [*Liu et al.*, 2010], by modulating the background atmosphere [*Chang et al.*, 2011], and by modulating the distribution of excitation sources such as stratospheric O_3 [*Goncharenko et al.*, 2012].

[3] Located within a similar range of altitudes as the MLT region is the ionosphere *E* region (between about 100 and 150 km), where the ion-neutral collision frequency is comparable with or larger than the gyrofrequency of ions ($\nu_i \gtrsim \omega_i$) while the electron-neutral collision frequency is much

[1]High Altitude Observatory, National Center for Atmospheric Research, Boulder, Colorado, USA.

Corresponding author: Y. Yamazaki, High Altitude Observatory, National Center for Atmospheric Research, 3080 Center Green Dr., Boulder, CO 80301, USA. (yamazaki@ucar.edu)

2169-9380/13/10.1002/jgra.50487

smaller than the gyrofrequency of electrons ($\nu_e \ll \omega_e$). In this region, therefore, ions are coupled with neutral wind while electrons are frozen to magnetic field lines. As a result of different motions between ions and electrons, electric currents are generated. In general, these wind-induced currents are not divergence-free, thus a polarization electric field is set up to maintain closure of total electric currents. These generation processes of electric fields and currents are known as the ionosphere wind dynamo [*Richmond*, 1979, 1989].

[4] At the magnetic equator, where magnetic field lines are completely horizontal, the polarization electric field is associated with vertical plasma drifts, which move plasma upward across magnetic field lines during daytime. In the *F* region, the plasma diffuses downward along magnetic field lines because of gravity and plasma pressure gradients [*Hanson and Moffett*, 1966]. This plasma transport process is often referred to as the equatorial plasma fountain. The result is a depletion of *F* region plasma density at the magnetic equator and two crests of plasma density on either side of the magnetic equator (about 15–20° away from the magnetic equator), which is known as the equatorial ionization anomaly (EIA). Although most tidal waves from the lower and middle atmosphere are not able to propagate into the *F* region ionosphere, they can influence the distribution of *F* region plasma by modulating the ionospheric *E* region wind dynamo and equatorial plasma fountain [*Millward et al.*, 2001]. *Chen et al.* [2008] compared daily values of ionospheric total electron content (TEC) at the EIA crests and the strength of the equatorial electrojet during magnetically quiet periods. The latter is a measure of the equatorial zonal electric field produced by the *E* region wind dynamo. The positive correlation ($r \sim 0.5$) they obtained partially supports the *E* region dynamo effect on the *F* region plasma density, but a large scatter indicates that there are other important factors at work. (Note that the positive correlation arises in part from a similar dependence of the two quantities on solar forcing.)

[5] The *F* region plasma density is also affected by the composition of the neutral atmosphere, from which ions and electrons are produced. At the altitude of the *F* region ionosphere, the neutral composition primarily consists of atomic oxygen O_1, molecular oxygen O_2, and molecular nitrogen N_2. The plasma population at *F* region heights is dominated by O^+, and its main source is photoionization of O_1,

$$O_1 + h\nu \rightarrow O^+ + e^-, \tag{1}$$

where $h\nu$ represents an extreme ultraviolet photon. Therefore, atomic oxygen leads to O^+ production. Meanwhile, loss of O^+ occurs mainly through ion-exchange reactions,

$$O^+ + N_2 \rightarrow NO^+ + N \tag{2}$$

and

$$O^+ + O_2 \rightarrow O_2^+ + O_1. \tag{3}$$

These are followed by a rapid dissociative recombination with electrons, so that NO^+ and O_2^+ are almost immediately destroyed,

$$NO^+ + e^- \rightarrow N + O_1 \tag{4}$$

and

$$O_2^+ + e^- \rightarrow O_1 + O_1, \tag{5}$$

respectively. Therefore, molecular species (N_2 and O_2) act to reduce ionospheric plasma density. If photochemical equilibrium existed, the electron density would be approximately proportional to the density ratio $[O_1]/[N_2]$, which is often used as a measure of thermospheric composition influence on the *F* region ionospheric plasma.

[6] Tidal effects on the neutral composition have been investigated by *Akmaev and Shved* [1980] and *Forbes et al.* [1993]. *Akmaev and Shved* [1980], based on a one-dimensional model, demonstrated that inclusion of tidal forcing causes a decrease of atomic oxygen in the MLT region. *Forbes et al.* [1993] confirmed this using a three-dimensional model. Furthermore, they found that the composition change extends to the upper part of the thermosphere and affects the distribution of *F* region plasma. Both authors suggested that the reduction of atomic oxygen in the MLT region is due to an increase in the effective three-body recombination rate of atomic oxygen, which would induce a net downward transport of atomic oxygen. (This mechanism will be explained in more detail later.) The effectiveness of this mechanism is, however, still to be investigated.

[7] A question to ask at this point is, "What is the net effect of upward-propagating tides on the ionosphere when effects of both the ionospheric wind dynamo and composition change are considered?" To answer this question, we carry out numerical experiments on the basis of the National Center for Atmospheric Research (NCAR) Thermosphere-Ionosphere-Electrodynamics General Circulation Model (TIE-GCM) [*Richmond et al.*, 1992]. Earlier, *Forbes et al.* [1993] studied tidal effects on the thermosphere and ionosphere using the Thermosphere-Ionosphere General Circulation Model (TIGCM) [*Roble et al.*, 1988], which is a predecessor version of the TIE-GCM. The TIGCM uses an electric field from an empirical model and neglects changes in the electric field and their feedback on the neutral and plasma motions. Also, the TIGCM uses a simple dipole magnetic field.

2. Models

[8] Most of our simulations are based on the TIE-GCM. The TIE-GCM is a three-dimensional time-dependent model of the coupled thermosphere and ionosphere. At each time step of 2 min, the model self-consistently solves for global electric fields and currents, neutral and ionized constituent densities, temperatures, and winds. (See *Dickinson et al.* [1981, 1984], *Roble et al.* [1988], *Richmond et al.* [1992], and L. Qian et al. (The NCAR TIE-GCM: A community model of the coupled thermosphere/ionosphere system, submitted to *Modeling the Ionosphere- Thermosphere*, 2013) for a detailed description of the model.) The horizontal resolution of the model is 5° by 5° in geographic longitude and latitude. The model uses constant-pressure surfaces as the vertical coordinate. The pressure interfaces are defined as $Z = \ln(P_0/P)$, where P is pressure and $P_0 = 5 \times 10^{-7}$ hPa. The upper and lower boundaries are at $Z = 7$ (4.6×10^{-10} hPa) and $Z = -7$ (5.5×10^{-4} hPa), respectively, and there are two grid points per scale height. The electrodynamics are calculated in the Magnetic Apex coordinate system [*Richmond*, 1995] using a realistic magnetic field (International Geomagnetic Reference Field). The TIE-GCM specifies solar XUV, EUV, and FUV spectral fluxes for a given solar radiation index *F*10.7 using the EUVAC model [*Richards et al.*, 1994]. *Fang et al.* [2008] pointed out, however, that the TIE-GCM with the EUVAC model underestimates *E* region

electron densities, as compared with the International Reference Ionosphere. They proposed to increase soft X-ray fluxes (wavelengths between 8 and 70 Å) by a factor of 4.4, which would achieve realistic *E* region plasma density with little impact on the *F* region plasma. *Solomon* [2006] pointed out that the agreement for the soft X-rays between the TIMED/SEE measurements and the EUVAC model is not as good as other wavelengths due to the difficulty of accurately measuring in the 8–70 Å range. Since our calculations include ionospheric currents, we use *Fang et al.*'s modification in order to have reasonably accurate daytime *E* region electrical conductivities.

[9] All our simulations are run in a perpetual March equinox condition (i.e., the calendar day is fixed at 80) for a moderate solar activity level ($F10.7$ is 120). At high latitudes, an external electric field is specified using an empirical electric potential model by *Heelis et al.* [1982] for a low geomagnetic activity condition with cross-polar-cap potential of 30 kV. The average altitudes of the upper and lower boundaries are 572 and 96 km in these conditions. At the lower boundary, tidal perturbations in winds, temperature, and geopotential height can be specified using the Global Scale Wave Model (GSWM) [*Hagan and Forbes*, 2002 and 2003]. Only migrating diurnal and semidiurnal tides from the GSWM are considered, and nonmigrating tides are neglected in this study. (The migrating tides are those which propagate westward at the same speed as the apparent motion of the Sun when observed from the ground, while all other tides are nonmigrating tides.) By comparing the results with and without lower-boundary forcing, it is possible to separate the effects of the tides locally generated at ionospheric heights from the effects of upward-propagating tides.

[10] Another model we use is the Thermosphere-Ionosphere-Mesosphere Electrodynamics General Circulation Model (TIME-GCM) [*Roble and Ridley*, 1994]. The TIME-GCM is an extended version of the TIE-GCM, having its lower boundary down at $Z = -17$ (approximately 30 km). The TIME-GCM incorporates all of the physical and chemical processes of the TIE-GCM, and it uses a 2.5° by 2.5° horizontal grid with four vertical grid points per scale height. At the TIME-GCM lower boundary, tidal perturbations can be specified using the GSWM, and it is possible to conduct simulations with and without lower-boundary tidal forcing. In the TIME-GCM, however, even when the lower-boundary tidal forcing is off, upward-propagating tides are excited in the upper stratosphere and mesosphere, some of which propagate into the ionosphere. Consequently, it is not possible, using the TIME-GCM, to evaluate the impact of the upward-propagating tides generated between the model lower boundary (∼30 km) and the bottom of the dynamo region (∼100 km) merely by calculating the differences between runs with and without GSWM tides at the lower boundary. Since our focus in this study is on the ionospheric response to upward-propagating tides from below, we mainly use the simpler TIE-GCM.

3. Results

3.1. Wind Fields

[11] We first examine changes in the thermospheric wind due to upward-propagating migrating tides. Figure 1 presents height versus latitude distributions of the wind amplitude for diurnal (top row) and semidiurnal (bottom row) tides derived from the TIE-GCM. The results within one scale height from the lower and upper boundaries are omitted because they could be affected by the boundary conditions. UN, VN, and WN in the figure denote eastward, northward, and vertically upward winds, respectively. The simulations are run for 40 days from the time lower-boundary forcing is switched on to obtain a diurnally reproducible state. The difference in the wind vectors computed with and without lower-boundary tidal forcing is derived so as to isolate the effects of upward-propagating tides from those locally generated in the thermosphere. Using the data for the last 24 h of the run, wind amplitudes for diurnal and semidiurnal migrating tides are determined based on least square fitting. In such an analysis, data for 24 h are required to separate migrating and nonmigrating tidal components. When the lower-boundary forcing is off, the main tidal component resolved in the model is the vertically non-propagating migrating diurnal component produced by solar ultraviolet heating in the thermosphere [*Hagan et al.*, 2001]. This tidal component is quite large at high altitudes (horizontal tidal wind amplitudes are typically over 100 m/s above $Z = -1$) but is not seen in Figure 1, because it is nearly identical for the runs with and without lower-boundary forcing.

[12] In Figure 1, the results for the upward-propagating migrating diurnal tide indicate the dominance of the (1,1) Hough mode of classical tidal theory [*Lindzen and Chapman*, 1969], with maximum horizontal wind amplitudes at ±20–30° latitude (top left and top middle panels). For the semidiurnal tide, peak amplitudes of the horizontal wind tide appear at 50° latitude, indicative of the dominance of the (2,4) Hough mode (bottom left and bottom middle panels). The altitude for the peak amplitude of the semidiurnal tide (approximately at 108 km) is higher than that of the diurnal tide (at 96–101 km). This is owing to the fact that the semidiurnal tide has a longer vertical wavelength and faster vertical group velocity [*Vial et al.*, 1991], and thus it can propagate to higher levels before being dissipated. Vertical wind tidal amplitudes are smaller than horizontal ones by 2 orders of magnitude (top right and bottom right panels). It is noted that tidal amplitudes and their distributions in the MLT region are in good agreement with those derived from satellite observations in the past [*Khattatov et al.*, 1997a, 1997b; *Wu et al.*, 2006]. (Although observations include contributions from both upward-propagating tides and the tides locally generated in the thermosphere, the comparison between the results in Figure 1 and observations is still valid in the MLT region because the amplitude of thermospherically generated tides is relatively small below 120 km.) A comparison of the upward-propagating migrating tides between the TIE-GCM and GSWM shows general agreement at altitudes of 100–140 km, with discrepancies in the wind amplitude of 10–40% (not shown). The difference in tidal amplitudes between the TIE-GCM and GSWM arises probably from different background fields and parameterizations used in the two models. Although we will not argue which model's tides are more correct, it is fair to say that there is uncertainty in the amplitude of the migrating tides in the MLT region. Therefore, it is important to bear in mind that the tidal effects we will show in this paper could be either more or less significant in the actual atmosphere.

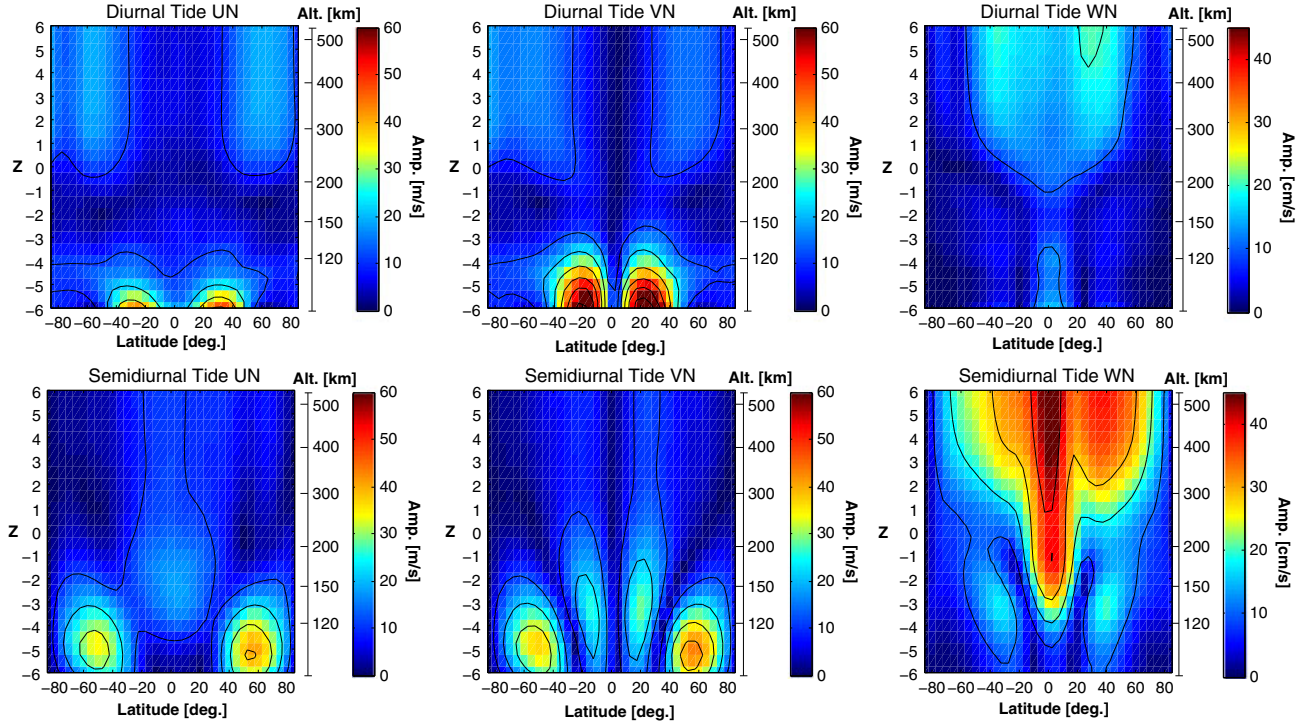

Figure 1. Wind amplitudes for upward-propagating migrating (top row) diurnal and (bottom row) semidiurnal tides, as derived from the difference in the neutral winds computed with and without lower-boundary forcing. Contour interval is 10 m/s for the (left column) eastward wind, (middle column) northward wind, and 10 cm/s for the (right column) upward wind.

[13] Dissipating tides deposit net momentum into the mean flow and modify the zonal-mean circulation in the lower thermosphere, just as planetary waves and gravity waves do in the stratosphere and mesosphere. This was first pointed out by *Miyahara* [1978] and has been established by more recent works [*Miyahara and Wu*, 1989; *Angelats i Coll and Forbes*, 2002; *Yoshikawa and Miyahara*, 2003]. Figure 2 illustrates zonal-mean winds induced by upward-propagating migrating tides. The results are, as in Figure 1, derived from the difference in the wind fields computed with and without lower-boundary tidal forcing. The top left and bottom left panels show the zonal-mean zonal wind generated by the upward-propagating diurnal and semidiurnal tides, respectively. A westward mean wind over the equator is evident in both cases. Observations have revealed a westward mean flow in the MLT region during the equinoxes [e.g., *Swinbank and Ortland*, 2003]. The top middle and top right panels depict the zonal-mean meridional circulation induced by the upward-propagating migrating diurnal tide. Below 120 km, a cell-like structure with poleward flow (7 m/s) on both sides of the equator is visible between $\pm 30^\circ$ latitude. The poleward mean meridional flow is consistent with the direction that would result from Coriolis deflection of the enhanced westward mean zonal flow in both hemispheres. Observations have reported a similar poleward mean flow at low latitudes below 110 km during the equinox [*McLandress et al.*, 1996; *Zhang et al.*, 2007]. Those observations, however, showed equatorward flow above 110 km, which is not found in our TIE-GCM results. The poleward mean flow also exists in the results for the semidiurnal tide (105–150 km), but with smaller velocity (bottom middle and bottom right panels).

3.2. Transient Ionospheric Response

[14] The response of the daytime ionosphere to the tidal forcing is examined using the TIE-GCM. Computed in the model are three ionospheric quantities that are commonly used in ionospheric studies: total intensity of the equivalent current system, upward velocity of the equatorial *F* region vertical plasma drift, and ionospheric total electron content (TEC) at the crests of the EIA.

[15] The equivalent current system is a horizontal thin-shell current system, which is equivalent to the actual three-dimensional ionospheric current system in that they would produce the same magnetic perturbations on the ground [*Chapman and Bartels*, 1940]. The equivalent current system gives a good approximation of the *E* region current system due to the fact that most of horizontal ionospheric currents flow at altitudes between 100 and 150 km. (The thickness of the dynamo region is less than 1% of the horizontal scale of the current system.) Morphology of the equivalent current system has been well established mainly through ground magnetometer observations [e.g., *Takeda*, 2002]. In the TIE-GCM, the equivalent current system is calculated using the method described by A. D. Richmond and A. Maute (Ionospheric electrodynamics modeling, submitted to *Modeling the Ionosphere- Thermosphere*, 2013). Past studies have shown that the TIE-GCM is able to reproduce the observed features of the equivalent current system [e.g., *Yamazaki et al.*, 2012a]. Total intensity of the

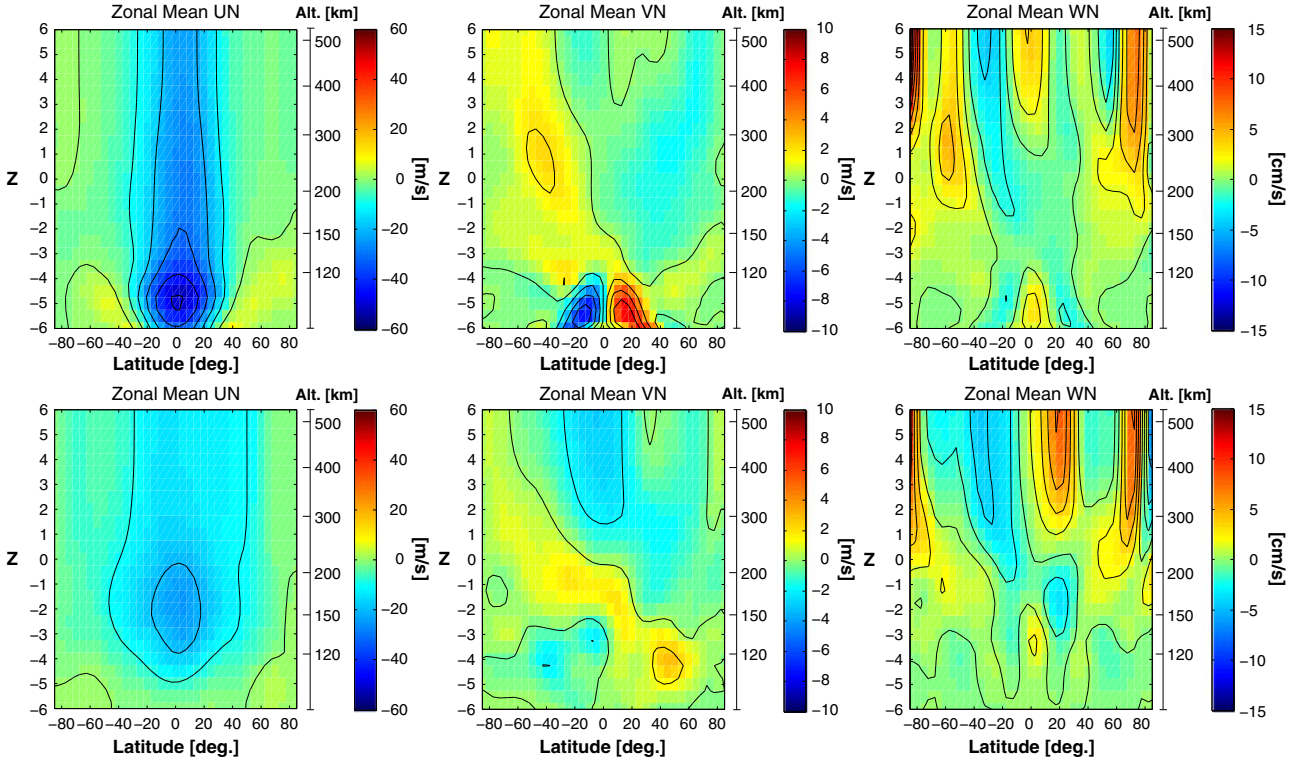

Figure 2. Zonal-mean winds induced by the upward-propagating migrating (top row) diurnal tide and (bottom row) semidiurnal tide at 00:00 UT, as derived from the difference in the neutral winds computed with and without lower-boundary forcing. Contour interval is 10 m/s for the (left column) eastward wind, 2 m/s for the (middle column) northward wind, and 2 cm/s for the (right column) upward wind.

equivalent current system J_{total} is defined as the difference between maximum and minimum values of the current (potential) function below 60° magnetic latitude. J_{total} is a measure of the total amount of wind dynamo currents flowing in the *E* region ionosphere.

[16] Equatorial *F* region vertical plasma drifts have been extensively studied in the past by ground and satellite observations [e.g., *Fejer and Scherliess*, 2001; *Fejer et al.*, 2008]. The quantity is important in understanding the distribution of ionospheric plasma because it contains information about vertical plasma transport. During the daytime, the drift is usually upward, which raises the *F* region. Comparisons between data and the TIE-GCM have shown that the model is capable of reproducing local time, seasonal, and solar-activity variations of the equatorial *F* region vertical plasma drifts [*Fesen et al.*, 2000; *Fang et al.*, 2008]. We computed in the TIE-GCM the noon-time vertical plasma drift velocity V_z at the magnetic equator at an altitude of 300 km. V_z is a measure of the eastward electric field in the equatorial ionosphere and also a measure of upward plasma transport through the equatorial plasma fountain.

[17] The TEC is also widely used for ionospheric surveys [e.g., *Jee et al.*, 2004]. TEC at a given location is defined as the total number of electrons in a column with a cross section of 1 m^2. It is dominated by electrons near the altitude of F2 layer peak (250–400 km). The TIE-GCM can reproduce vertical and horizontal distributions of the electron density [*Fesen et al.*, 2002; L. Qian et al., submitted manuscript, 2013]. We produce a global TEC map using the TIE-GCM to determine the location and magnitude of the crests of the EIA. TEC in the model is computed by integrating the electron density from the lower boundary (approximately 96 km) to 500 km. The TEC values at the northern and southern crests of the EIA are averaged, which we call $\text{TEC}_{\text{crest}}$. $\text{TEC}_{\text{crest}}$ is a measure of the electron density in the *F* region ionosphere at low latitudes. It may be noted that $\text{TEC}_{\text{crest}}$ derived from the model is not directly comparable with those derived from ground observations that contain contributions from the plasmasphere.

[18] We conduct a continuous 50 day run of the TIE-GCM to examine the transient response of the ionosphere to upward-propagating migrating diurnal and semidiurnal tides. J_{total}, V_z, and $\text{TEC}_{\text{crest}}$ are output at 00:00 UT of each model day. Tidal forcing at the lower boundary is kept off for the first 10 days. It is then turned on at 01:00 UT of the tenth day and kept on for the rest of the period. The results are presented in Figure 3. In each panel, the black line indicates the case where both migrating diurnal and semidiurnal tides from the GSWM are used for the lower-boundary forcing. The red/blue line is for the case where only the migrating diurnal/semidiurnal tide is used. The simulations are carried out under equinoctial conditions, and the advance of calendar day is not taken into account so that seasonal variations will not affect the results. We note that the results at different UTs are basically the same but with slightly different offset values.

[19] The results in Figure 3 reveal almost step-like increases in J_{total} and V_z in response to the tidal forcing. Increases in the electric fields and currents due to upward-propagating semidiurnal tides were reported earlier

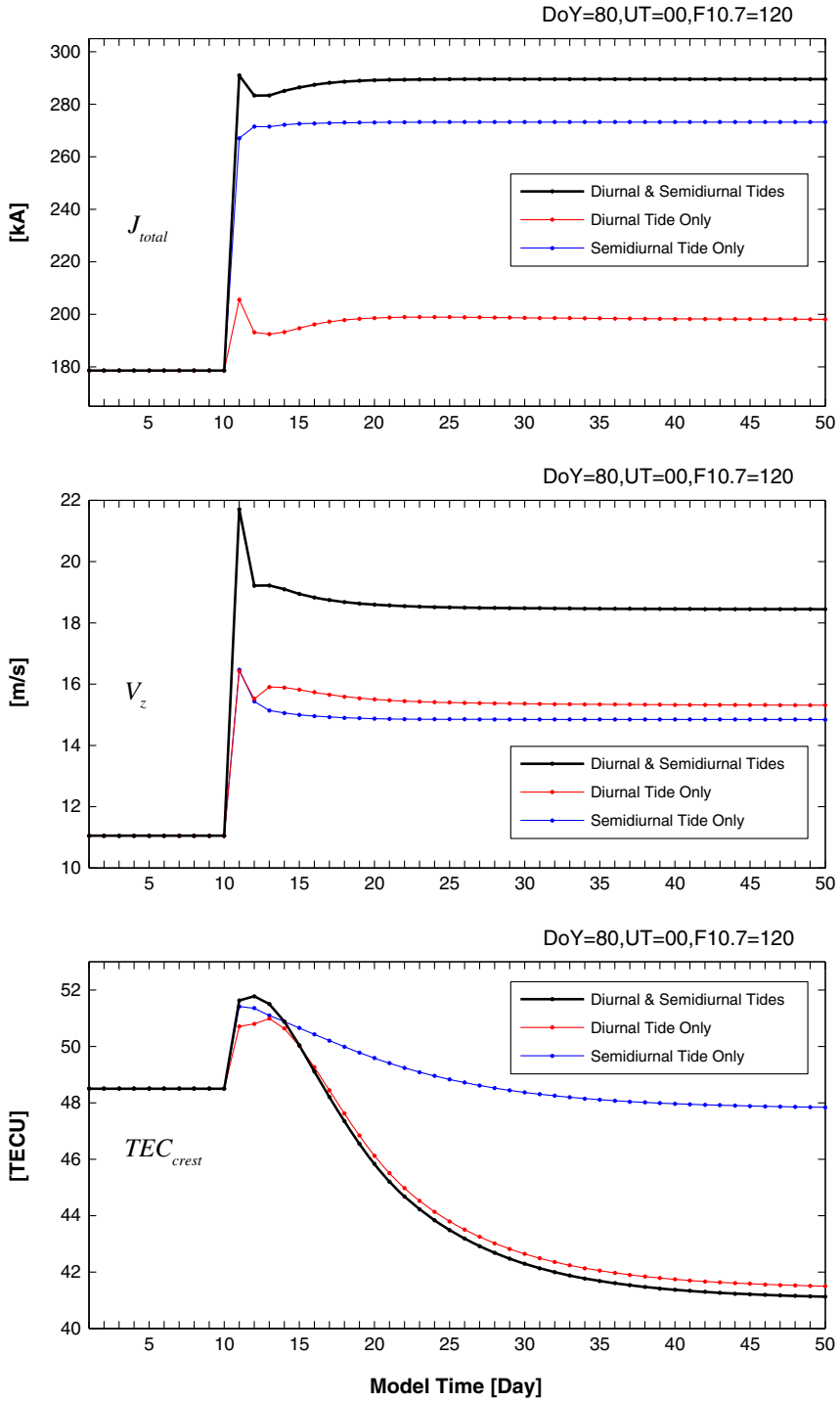

Figure 3. (top) Total intensity of the equivalent current system J_{total}, (middle) upward velocity of the equatorial F region ionospheric drift V_z, and (bottom) averaged total electron content at the crests of the EIA $\text{TEC}_{\text{crest}}$ at 00:00 UT. Tidal forcing at the lower boundary is turned on at 01:00 UT of Day 10. The black lines indicate the case where both migrating diurnal and semidiurnal GSWM tides are used for the lower-boundary forcing. The red/blue lines indicate the case where only the migrating diurnal/semidiurnal GSWM tide is used. One TEC unit (TECU) is equal to 10^{16} electrons per m^2. Note that the vertical scales do not start at zero.

by *Richmond and Roble* [1987]. The increase in J_{total} (by approximately 60%) is mostly due to the semidiurnal tide, and the contribution of the diurnal tide is relatively small. A reason for this is the height distribution of ionospheric conductivity. The Hall conductivity is greatest at an altitude of approximately 110 km, which is around where the semidiurnal tidal wind achieves its maximum amplitude. Meanwhile, the altitude for the maximum diurnal tidal wind

is lower at about 100 km, where the conductivities are relatively small.

[20] For the increase in V_z (by approximately 70%), both the diurnal and semidiurnal tides are equally important in this simulation result. Under equinoctial conditions, both the diurnal and semidiurnal tides are dominated by symmetric modes, which are effective in generating an electric field. Symmetric tidal modes will exhibit zonal winds of the same direction in the northern and southern hemispheres, while meridional winds in both hemispheres will either be identically poleward or identically equatorward.

[21] Differences exist in the results for J_{total} and V_z as to how they respond to the diurnal and semidiurnal tides. In the ionospheric wind dynamo theory, electric fields and currents are not proportional to each other but their relationship depends on the distribution of the driving wind. In principle, some wind distributions can produce electric currents without producing electric fields while other wind distributions can produce an electric field without producing electric currents [*Richmond*, 1979, and references therein].

[22] The $\text{TEC}_{\text{crest}}$ shows a different response to the upward-propagating tides in comparison to J_{total} and V_z. It first increases, then gradually decreases to below the initial level. After the tidal forcing is imposed, approximately 30 days are required to reach a new steady state, where $\text{TEC}_{\text{crest}}$ is approximately 15% lower than the initial state. Both the diurnal and semidiurnal tides produce the initial increase in $\text{TEC}_{\text{crest}}$, while the subsequent decrease in $\text{TEC}_{\text{crest}}$ is due in large part to the diurnal tide.

[23] The initial increase in $\text{TEC}_{\text{crest}}$ can be explained as a result of the increased equatorial plasma fountain. That is, the enhanced V_z by tidal forcing increases upward transport of plasma at the magnetic equator. The plasma then diffuses downward along magnetic field lines, causing an increase in the plasma density at the crests of the equatorial anomaly. This is well illustrated in Figure 4, which shows latitude profiles of electron density at an altitude of 400 km for Days 01, 12, and 50 from the same model run as for Figure 3. The results are for 15:00 LT, around when TEC reaches its greatest value. Compared to the result for Day 01, the electron density for Day 12 is lower at the magnetic equator and higher at the crests of the equatorial anomaly. The enhanced equatorial plasma fountain removes plasma at the magnetic equator by transporting it to higher latitudes. Comparison between the results for Day 01 and Day 12 also indicates a poleward shift of the crests of the equatorial anomaly. This is consistent with the observation results by *Balan and Iyer* [1983] and *Rastogi and Klobuchar* [1990], who demonstrated that a stronger equatorial electrojet corresponds to an equatorial anomaly crest at a higher latitude. The electron density for Day 50 is lower than Day 12 at all latitudes.

[24] The decrease in $\text{TEC}_{\text{crest}}$ is due to changes in the neutral composition. Figure 5 shows the percent difference in zonal mean $[O_1]/[N_2]$ ratio (left) and neutral temperature (right) between Day 01 and Day 50. At altitudes for the F region ionosphere (above 200 km), tidal forcing causes a reduction in the $[O_1]/[N_2]$ ratio by 20–30%, which can explain the decrease of $\text{TEC}_{\text{crest}}$ in Figure 3. The decrease in the $[O_1]/[N_2]$ ratio can be seen everywhere except middle to high latitudes (above 40°) below 110 km. The effect of the upward-propagating tides on the zonal-mean temperature is relatively small. The maximum change in the zonal-mean

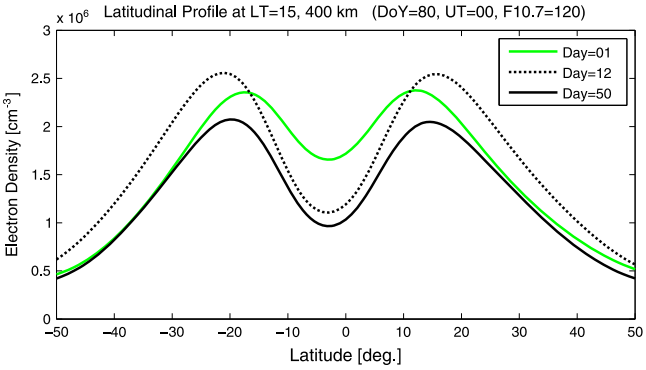

Figure 4. Latitude profile of the electron density at an altitude of 400 km. The results at a longitude sector corresponding to 15:00 LT (at 00:00 UT) are shown. The green line is the result for Day 01, when the lower-boundary forcing is off. The black dashed and solid lines are the results for Day 12 and Day 50, respectively, which are after the lower-boundary forcing (including both migrating diurnal and semidiurnal GSWM tides) is turned on at 01:00 UT of Day 10.

temperature is only a few percent, which indicates that the temperature changes are not directly responsible for the decrease in the $[O_1]/[N_2]$ ratio.

[25] The results for the neutral composition may be influenced by the lower-boundary conditions, which are imposed inside the MLT region and are somewhat artificial. We consider this effect. In the TIE-GCM, three major neutral constituents of the thermosphere are taken into account: O_1, O_2, and N_2. The mass mixing ratio of each constituent is defined as the relative mass density; for example, the mass mixing ratio of atomic oxygen is given as

$$\psi_{O_1} = \frac{\rho_{O_1}}{\rho_{O_1} + \rho_{O_2} + \rho_{N_2}}, \tag{6}$$

where ρ_{O_1}, ρ_{O_2}, ρ_{N_2} denote the mass densities of O_1, O_2, and N_2, respectively. At the lower boundary of $Z = -7$, the model requires the mass mixing ratios of the major species to satisfy the following conditions [*Dickinson et al.*, 1984]:

$$\frac{\partial \psi_{O_1}}{\partial Z} = \psi_{O_1} \tag{7}$$

$$\psi_{O_2} = 0.22. \tag{8}$$

The lower-boundary condition for ψ_{O_1} derives from the observation that the atomic oxygen concentration peaks around the mean height of the TIE-GCM lower boundary, and thus the vertical gradient of O_1 density there becomes zero, i.e., $\frac{\partial [O_1]}{\partial Z} = 0$, which leads to (7). However, this treatment can be problematic. For example, when tidal perturbations are introduced at the lower boundary, the altitude of the lower boundary varies, and the lower-boundary conditions (7) and (8) act to induce unrealistic transport through the lower boundary.

[26] To provide insight into how much the lower-boundary conditions affect the composition results, we carry out a similar calculation but using the TIME-GCM. Compared to the TIE-GCM, the TIME-GCM has the lower boundary at a much lower height of $Z = -17$ (approximately 30 km), and the artificial boundary conditions for the

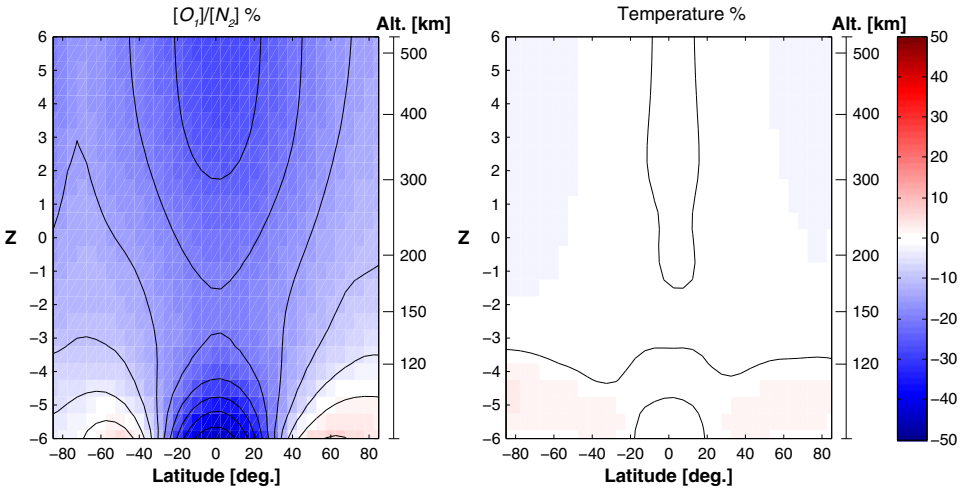

Figure 5. Percent difference in the zonal mean $[O_1]/[N_2]$ ratio (left) and temperature (right) computed with and without the lower-boundary forcing (including both migrating diurnal and semidiurnal GSWM tides). Contour interval is 5%.

thermospheric composition do not exist. TIME-GCM simulations are carried out with and without lower-boundary tidal forcing, which is specified as migrating diurnal and semidiurnal tides from the GSWM. Other external boundary conditions are set to be the same as our TIE-GCM calculations, i.e., calendar day is 80; $F10.7$ is 120; and cross-polar-cap potential is 30 kV. The difference in the zonal mean $[O_1]/[N_2]$ ratio calculated with and without lower-boundary tidal forcing is shown in Figure 6, confirming the reduction in the $[O_1]/[N_2]$ ratio due to upward-propagating tides. Although, as we noted earlier, tidal effects evaluated by the TIE-GCM and TIME-GCM are not directly comparable, the qualitative agreement of the composition results from the two models gives us confidence that the composition changes due to tides in the TIE-GCM are not artificial effects resulting from the lower-boundary conditions. Causes for the decrease in the zonal mean $[O_1]/[N_2]$ ratio will be examined in the following section using the TIE-GCM.

3.3. Tidal Mixing

[27] Figure 7 shows the global mean mass mixing ratio of major species with and without lower-boundary tidal forcing. The results show a decrease in atomic oxygen and increase in molecular species due to tidal forcing at almost all heights. This is consistent with prior results by *Akmaev and Shved* [1980] and *Forbes et al.* [1993]. Those studies suggested that tides produce a mixing effect, e.g., a similar effect as would be produced if the eddy diffusion coefficient is increased. We found that a TIE-GCM simulation without lower-boundary tidal forcing but with the eddy diffusion coefficient increased by 1.5 times gives almost the same results as Figure 7 (not shown). Recently, *Qian et al.* [2009] were able to reproduce seasonal variations in the $[O_1]/[N_2]$ ratio by modifying the eddy diffusivity used in the TIE-GCM. They multiplied the model eddy coefficient by seasonally varying factors of about 0.3–2.0, attributing it to the seasonal variation in turbulence caused by gravity waves coming from the middle atmosphere. Our results indicate that the presence of upward-propagating migrating tides has a comparable impact on the thermospheric composition.

[28] How do upward-propagating migrating tides produce the mixing effect in the model thermosphere? To provide some idea for possible mechanisms, we look into the neutral composition equation of the model. In the TIE-GCM, the time derivative of the mass mixing ratios of O_1 and O_2 is expressed as a sum of these compositional forcing terms: molecular diffusion, eddy diffusion, advection, and sources and sinks. That is,

$$\frac{\partial \Psi}{\partial t} = T_{\mathrm{MD}} + T_{\mathrm{ED}} + T_{\mathrm{AV}} + T_{\mathrm{SS}}, \tag{9}$$

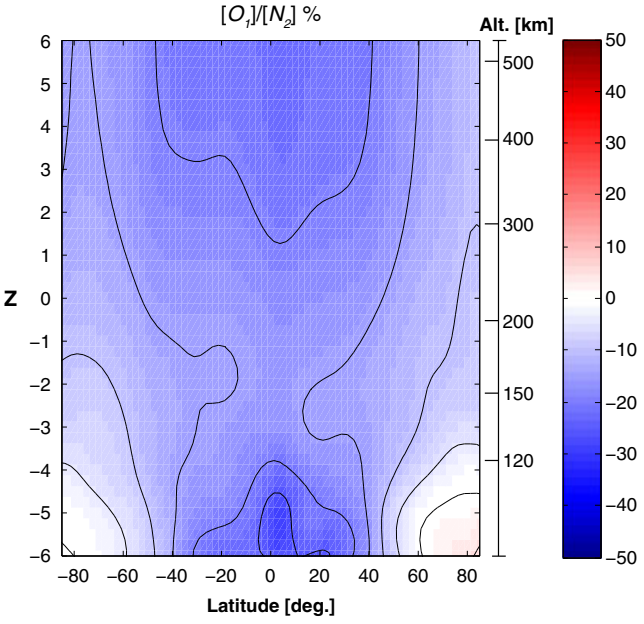

Figure 6. Same as the left panel of Figure 5 but simulated by the TIME-GCM.

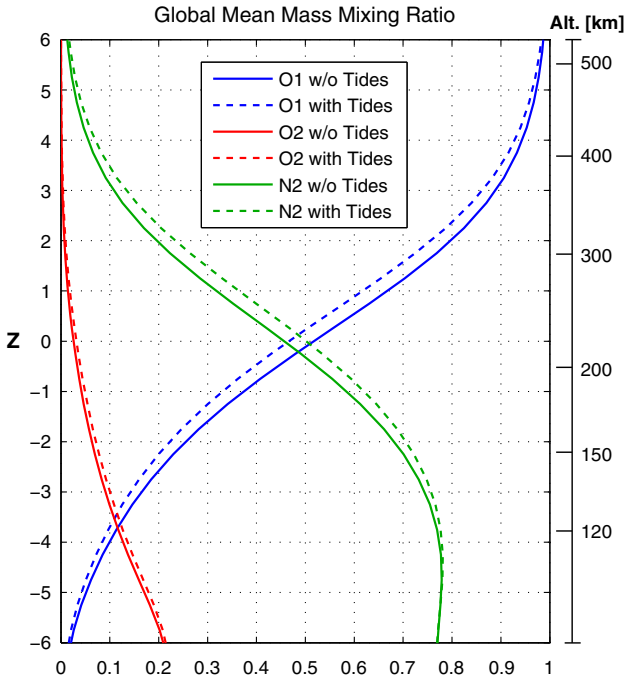

Figure 7. Height profile for global mean mass mixing ratio of O_1 (blue), O_2 (red), and N_2 (green). The dashed/solid line indicates the results computed with/without the lower-boundary forcing (including both migrating diurnal and semidiurnal GSWM tides).

where Ψ is a mass mixing ratio vector $\begin{pmatrix} \psi_{O_2} \\ \psi_{O_1} \end{pmatrix}$, and by definition ψ_{N_2} is given as $1 - \psi_{O_1} - \psi_{O_2}$. (See *Dickinson et al.* [1984] and references therein for a full mathematical description of the equation.) The molecular diffusion term T_{MD} represents the tendency for the mass mixing ratio to maintain a state of diffusive equilibrium in the vertical direction. T_{MD} involves mutual molecular diffusion coefficients $D(O_1, O_2)$, $D(O_1, N_2)$, and $D(O_2, N_2)$ in units of m^2 s^{-1}, which are given by *Colegrove et al.* [1966] as follows:

$$D(O_1, O_2) = 0.26 \times 10^{-4} \left[\frac{P_{00}}{P}\right] \left[\frac{T}{T_{00}}\right]^{1.75} \quad (10)$$

$$D(O_1, N_2) = 0.26 \times 10^{-4} \left[\frac{P_{00}}{P}\right] \left[\frac{T}{T_{00}}\right]^{1.75} \quad (11)$$

$$D(O_2, N_2) = 0.18 \times 10^{-4} \left[\frac{P_{00}}{P}\right] \left[\frac{T}{T_{00}}\right]^{1.75}, \quad (12)$$

where T is the temperature, $P_{00} = 10^3$ hPa, and $T_{00} = 273$ K. From (10)–(12), it is understood that the molecular diffusion term T_{MD} becomes more significant with increasing height as the pressure exponentially decreases. Meanwhile, the eddy diffusion term T_{ED} of (9) represents the tendency for the mass mixing ratio to be independent of height as the effect of turbulence or small-scale eddy motion provides mixing of the thermospheric constituents. T_{ED} involves the eddy diffusive coefficient D_E in units of m^2 s^{-1}, which is given by *Dickinson et al.* [1984] as

$$D_E = 4.56 \times 10^{-9} H^2 \left[\frac{P}{P_0}\right], \quad (13)$$

where H is the scale height of the neutral gas in meters. In contrast to the molecular diffusion term T_{MD}, the eddy diffusion term T_{ED} is significant only near the lower boundary of the model and loses its importance with increasing height. The advection term T_{AV} of (9) is given as

$$T_{AV} = -\left(\mathbf{V} \cdot \nabla_H \psi + w \frac{\partial \psi}{\partial Z}\right), \quad (14)$$

where $\mathbf{V}$ is the horizontal velocity along a constant-pressure surface, ∇_H is the horizontal nabla operator, and w is the nondimensional vertical motion dZ/dt. T_{AV} represents the effect of neutral winds acting on preexisting gradients of mass mixing ratios, which changes the distribution of constituents. The sources and sinks term T_{SS} of (9) represents production and loss of each constituent through various chemical reactions. (See *Roble* [1995] for the chemical reactions involved.)

[29] We conduct a series of numerical experiments (Cases 1 to 5) using the TIE-GCM in order to identify the mechanism for tidal mixing. In those runs, modified versions of (9) are used to test possible tidal mixing mechanisms. For each experiment, the global mean mass mixing ratio of O_1 is computed with and without lower-boundary forcing, and the impact of upward-propagating migrating tides is evaluated by examining the difference. For simplicity, only the migrating diurnal tide from the GSWM is used for lower-boundary forcing. The simulations with and without lower-boundary forcing are run until a diurnally reproducible state is reached. Figure 8 shows the difference between the global mean mass mixing ratio of O_1 computed with and without lower-boundary forcing for each experiment. Descriptions for each

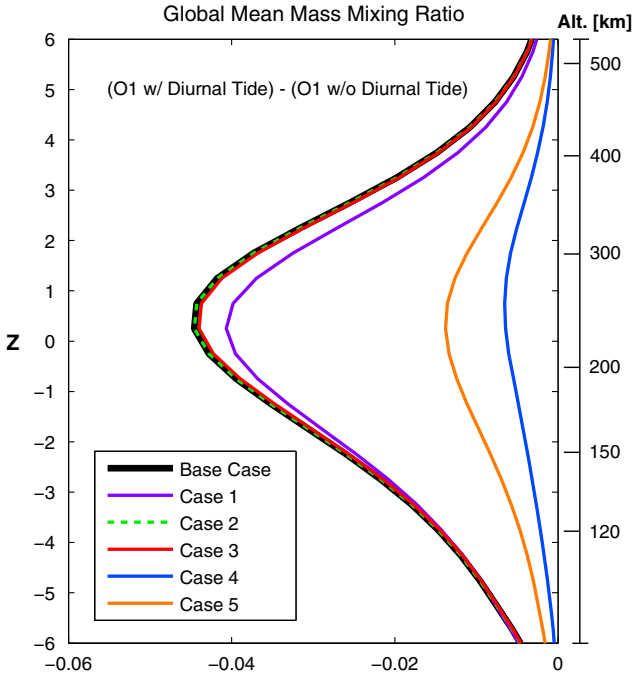

Figure 8. Difference in the global mean mass mixing ratios of O_1 computed with and without lower-boundary forcing of migrating diurnal GSWM tide. Different lines indicate the results from different TIE-GCM experiments. See the text in section 3.3 for description of each experiment.

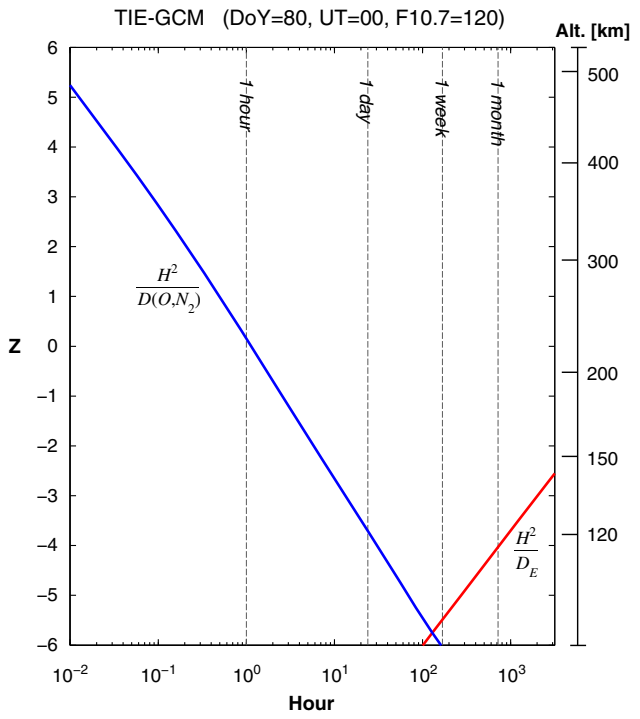

Figure 9. Height profile for characteristic time scales (global mean) of molecular diffusion $H^2/D(O_1, N_2)$ (blue) and eddy diffusion H^2/D_E (red). $H^2/D(O_1, N_2)$ gives a rough estimation for the time scale required to achieve diffusive separation. Meanwhile, $H^2/D(O_1, N_2)$ gives a rough estimation for the time scale required to achieve turbulent mixing.

experiment will be provided later. The "base case" is a reference TIE-GCM simulation without any change in (9). The result for the base case demonstrates a reduction in O_1 at all heights due to upward-propagating diurnal tide.

3.3.1. Case 1: Mixing Height

[30] *Müller-Wodarg and Aylward* [1998] argued that, at the heights where diffusive separation occurs faster than the time scale of tidal oscillations (hours), tides cannot upset a state of diffusive equilibrium. They thus postulated that tidal mixing is effective only in the lower part of the thermosphere where the diffusive separation occurs slowly compared to the period of tides. Here we consider their hypothesis and verify it through a TIE-GCM experiment (Case 1).

[31] As we have mentioned, molecular and eddy diffusion processes are strongly height dependent. To illustrate their dependence on height, we plot in Figure 9 the characteristic time scales for molecular and eddy diffusion. A characteristic time scale for the molecular diffusion is estimated as $H^2/D(O_1, N_2)$ [*Müller-Wodarg and Aylward*, 1998]. This gives the time required to largely return toward a state of diffusive equilibrium after being disturbed. Similarly, a time scale for the eddy diffusion is estimated as H^2/D_E. This gives the time required to achieve a large amount of turbulent mixing. It can be seen in Figure 9 that diffusive separation takes about 1 week at $Z = -6$ (approximately 100 km) and it gets faster with increasing height. Above $Z = -3$ (approximately 135 km), it takes less than 1 day to move substantially toward diffusive equilibrium. The time scale for turbulent mixing is comparable with diffusive separation at $Z = -6$, but it is much slower at greater heights.

[32] If *Müller-Wodarg and Aylward*'s hypothesis is right, the diurnal tide above $Z = -3$ or so is not effective in producing composition changes because diffusive separation there occurs so fast that diffusive equilibrium is always maintained despite tidal oscillations. To verify this, we conduct a numerical experiment (Case 1) where the amplitude of tidal oscillations is significantly reduced at $Z \geq -3$. The damping of the tidal amplitude is achieved by introducing a linear damping term (or Rayleigh friction term) to the momentum equation. The Rayleigh friction rate in s^{-1} is set to zero below $Z = -4$ and 10^{-2} above $Z = -3$, and there is an exponential increase between them. This significantly reduces tidal amplitudes in all dynamical fields above $Z = -3$, which will be reflected in (9) and affect the neutral composition. When lower-boundary tidal forcing is off, inclusion of the Rayleigh friction term effectively suppresses the amplitude of the tides locally generated in the thermosphere at $Z \geq -3$, but we found that this makes little change in the global mean mass mixing ratio of the major species, which indicates that the diurnal tide locally generated in the thermopshere contributes little to mixing. Figure 10 illustrates the impact of inclusion of the Rayleigh friction term on the upward-propagating migrating diurnal tide and zonal-mean winds induced by it. The figure shows the difference between the wind fields computed with and without lower-boundary forcing for Case 1. The top and bottom rows show tidal amplitudes and zonal-mean winds, respectively. From comparison with the base case results in Figures 1 and 2, one can see that tidal amplitudes and zonal-mean winds are significantly reduced at $Z \geq -3$ while they are almost the same below $Z = -3$.

[33] Tidal effects on the global mean ψ_{O_1} for Case 1 can be found in Figure 8. Although, in Case 1, there is practically no tidal oscillations above $Z \geq -3$ (Figure 10), the O_1 reduction still exists at all heights to a similar extent as the base case. Our results support *Müller-Wodarg and Aylward*'s hypothesis that most of the tidal mixing occurs in the lower part of the thermosphere where the diffusive separation is comparable with or slower than the time scale of tidal oscillations. At $Z \geq -3$, the composition at each height level changes according to composition changes at the level below so as to maintain a state of diffusive equilibrium.

3.3.2. Case 2: Increase in Effective Recombination Rate of O_1

[34] Next, a mechanism suggested by *Akmaev and Shved* [1980] is considered. They argued that the effective recombination rate of O_1 is enhanced in vertical tidal oscillations, which induces an increase in downward diffusion of O_1. In the thermosphere, loss of O_1 occurs mainly through three-body recombination,

$$O_1 + O_1 + M \rightarrow O_2 + M, \tag{15}$$

where M is either O_2 or N_2. In a tidal oscillation, an air parcel experiences both upward and downward vertical displacements from a constant-pressure surface during an oscillation cycle. When the air parcel is displaced up, the background pressure decreases and thus the density of the air parcel decreases, which slows down the recombination of O_1 described in (15). In contrast, when the air parcel is

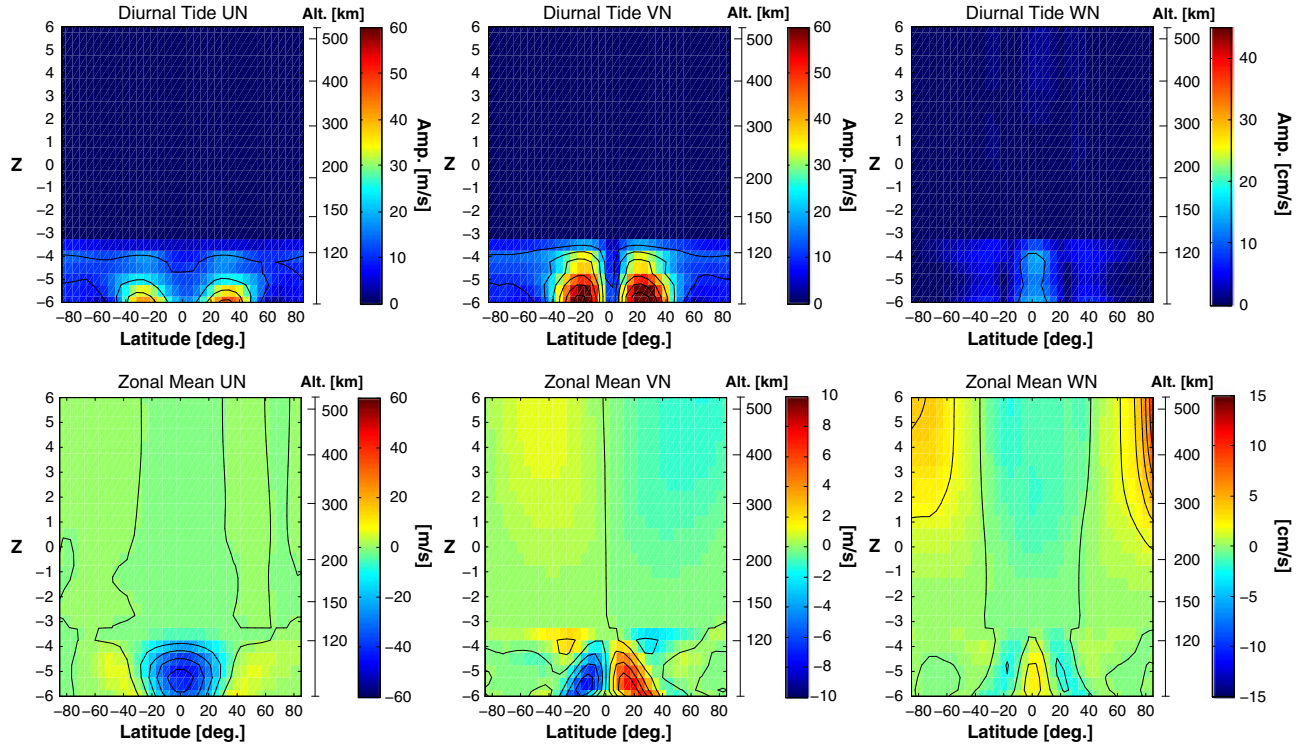

Figure 10. (top row) Wind amplitudes for the upward-propagating migrating diurnal tide in Case 1, as derived from the difference in the neutral winds computed with and without lower-boundary forcing. Contour interval is 10 m/s for the eastward wind (left) and northward wind (middle), and 10 cm/s for the upward wind (right). (bottom row) Zonal-mean winds induced by the migrating diurnal tide at 00:00 UT in Case 1, as derived from the difference in the neutral winds computed with and without lower-boundary forcing. Contour interval is 10 m/s for the eastward wind (left), 2 m/s for the northward wind (middle), and 2 cm/s for the upward wind (right).

displaced down, the O_1 recombination rate increases because of an increase in the density. Since the recombination rate varies with the cube of the atmospheric density as the air parcel is compressed or dilated, the increase and decrease of the O_1 recombination rate in one cycle do not balance; the result is an increase in the net recombination rate of O_1. Accordingly, the downward diffusion of O_1 will increase owing to the increased upward gradient of O_1 density. The downward transport of O_1 reduces the O_1 density at higher altitudes. The effectiveness of this mechanism was, however, not previously evaluated.

[35] In the TIE-GCM, loss of O_1 and production of O_2 through three-body recombination is included in the sources and sinks term T_{SS} of (9) in the form of $-2k\left(m_{O_1}/m\right)[O_1]^2$ and $k\left(m_{O_2}/m\right)[O_1]^2$, respectively, where k is a rate constant $9.59 \times 10^{-34} \exp[\frac{480}{T}]$, m is the mean molecular mass, m_{O_1} is the mass of O_1, m_{O_2} is the mass of O_2, and $[O_1]$ is the number density of O_1. We conduct a TIE-GCM experiment (Case 2) where these two terms in T_{SS} are replaced by their zonal averages below $Z = -3$ so that the increase in the effective recombination rate of O_1 due to tidal oscillations will not occur in the lower thermosphere. It is confirmed that this treatment has little influence on the global mean mass mixing ratio of the major species when lower-boundary tidal forcing is off. If the mechanism by *Akmaev and Shved* [1980] is of great importance, the O_1 reduction due to lower-boundary tidal forcing will not occur in Case 2. The result for Case 2 in Figure 8 is, however, very close to that of the base case, which means that *Akmaev and Shved*'s mechanism does not effectively produce the mixing effect due to the diurnal tide.

[36] The characteristic time scale for the O_1 recombination (in s^{-1}) may be estimated as follows:

$$\frac{\psi_{O_1}}{2k\left(m_{O_1}/m\right)[O_1]^2} \tag{16}$$

It is found that the recombination time scale is on the order of 100 days in the lower thermosphere and slower at greater heights (not shown). This is very slow compared to the time scale of tidal oscillations (hours) and the diffusion time scale in the lower thermosphere (see Figure 9). The slow rate of O_1 recombination is probably the reason why *Akmaev and Shved*'s mechanism is not effective in producing the mixing effect.

3.3.3. Case 3: Increase in Effective Vertical Diffusivity

[37] Tidal oscillations also increase the effective molecular and eddy diffusivity. Its importance in tidal mixing is considered in Case 3. As shown in Figure 7, the mass mixing ratio of O_1 increases with increasing height. Owing to this fact, when an air parcel is displaced up in a tidal oscillation, its O_1 mass mixing ratio is lower than that of adjacent air, and diffusion acts to add O_1 to the air parcel. When the air parcel is displaced down, diffusion acts to remove O_1 from it. For O_2 and N_2, diffusion acts in the opposite manner

because their mass mixing ratios tend to decrease with increasing height (Figure 7). Therefore, the net effect is a downward transport of atomic oxygen along with an upward transport of molecular species, analogous to an increase in diffusivity. The effectiveness of this O_1 transport mechanism is tested in a TIE-GCM experiment (Case 3). In Case 3, the molecular diffusion term T_{MD} of (9) is replaced by its zonal average below $Z = -3$ so as to substantially turn off the transport due to an increase in the effective molecular diffusivity. We found that this treatment makes little difference in the global mean mass mixing ratio of the major species when lower-boundary forcing is off. The tidal effect on the global mean O_1 mixing ratio for Case 3 is shown in Figure 8. The result for Case 3 is, again, close to that of the base case, indicating that the increase in the effective vertical diffusivity is not sufficient to explain the increased downward O_1 transport. Another experiment in which the eddy diffusion term T_{ED} of (9) is replaced by its zonal average below $Z = -3$ gives similarly small effects on the global mean O_1 mixing ratio, and the result is omitted from Figure 8.

3.3.4. Case 4: Role of Mean Meridional Circulation

[38] As shown in Figure 2 (top middle and top right panels), a mean meridional circulation is induced in the MLT region due to dissipating tides. In Case 4, the role of the mean meridional circulation in tidal mixing is investigated. A TIE-GCM experiment is carried out, where the northward wind VN and vertical motion w of (14) are replaced, below $Z = -3$, by $VN - \overline{VN}$ and $w - \overline{w}$, respectively, where the parameters with an overbar denote the zonal mean. In Case 4, therefore, the neutral composition described in (9) is not influenced by the mean meridional circulation in the MLT region but only by the oscillatory tidal winds. We found that, when lower-boundary forcing is off, the removal of the mean meridional circulation has little impact on the global mean mass mixing ratio of major species. The results in Figure 8 reveal that the elimination of transport by the mean meridional circulation reduces the net influence of the diurnal tide on O_1 by 80–90%. This indicates that the tidally-induced mean meridional circulation is acting like a large-scale turbulent eddy in the MLT region, producing the mixing effect that enhances net downward transport and loss of O_1.

[39] It should be noted that, in our analysis, the mean meridional circulation is considered on constant-pressure surfaces (thus the Eulerian mean), which is not exactly the same as the actual zonal-mean motion of air parcels (the Lagrangian mean). The difference between the Eulerian and Lagrangian means in the MLT region is discussed by *Watanabe et al.* [1999]. In general, the determination of the Lagrangian mean in a numerical model is technically difficult and beyond the scope of this paper. However, the fact that the Eulerian mean meridional circulation can explain most of the tidal mixing effects in the TIE-GCM is strongly suggestive of the principal role for the mean meridional circulation in tidal mixing, and thus the difference between the Eulerian and Lagrangian means may not be significant in the TIE-GCM.

3.3.5. Case 5: Dependence of Tidal Mixing on Tidal Amplitude

[40] To understand the dependence of tidal mixing on the amplitude of upward-propagating migrating diurnal tides, we carried out a TIE-GCM simulation (Case 5) where the amplitude of the lower-boundary tide is reduced by half. The results in Figure 8 show that the O_1 reduction in Case 5 is approximately 25–30% that of the base case. Hence, the extent of tidal mixing is not linearly proportional to the tidal amplitude but it tends to be proportional to the square of the tidal amplitude. This tendency is probably due to the fact that the zonal-mean wind induced by dissipating tides is dependent on the Eliassen-Palm (EP) flux of zonal momentum by the tide. Like the tidal energy flux, the EP flux tends to scale as the square of the wind amplitude.

4. Summary and Discussion

[41] The daytime ionospheric response to upward-propagating tides has been examined using the TIE-GCM, which can self-consistently compute the ionospheric wind dynamo along with the dynamics of the thermosphere and ionosphere in a realistic geomagnetic field. Simulations were carried out for equinox and magnetically quiet conditions with moderate level of solar activity ($F10.7 = 120$). The impact of upward-propagating tides on E region currents J_{total}, equatorial F region vertical plasma drift V_z, and total electron content at the EIA crests TEC_{crest} has been evaluated by forcing the model with GSWM migrating tides at the lower-boundary height of 96 km, which imitate the effects of upward-propagating tides from below.

[42] When the lower-boundary tides are added, both J_{total} and V_z showed a step-like increase by some 70% (Figure 3). This is because upward-propagating tides generate additional electric fields and currents, strengthening preexisting electric fields and currents that are mainly produced by the tides locally generated in the thermosphere. Meanwhile, TEC_{crest} first increased, then gradually decreased to below the initial level by 15% (Figure 3). The initial increase in TEC_{crest} can be explained as a result of an enhanced equatorial plasma fountain. That is, the electric field induced by upward-propagating tides enhances the daytime upward plasma transport at the magnetic equator, which is accompanied by downward and poleward diffusion of F region plasma to low latitudes along the magnetic field lines. The gradual decrease in TEC_{crest} arises from changes in the neutral composition due to tidal mixing of major species in the thermosphere.

[43] We have conducted further numerical experiments to identify the tidal mixing mechanism. The results confirmed the hypothesis of *Müller-Wodarg and Aylward* [1998]. That is, the tidal mixing is effective only in the lower part of the thermosphere where the diffusion separation occurs relatively slowly compared to the time scale of the tide (hours). Therefore, the composition changes arising from tidal forcing at F region heights are not dependent on the tide there but they are controlled by tidal mixing in the lower thermosphere. Furthermore, it was found that a mechanism suggested by *Akmaev and Shved* [1980], in which the mixing effect is basically explained by downward O_1 transport that results from the increase in the effective recombination rate of O_1, is not effective for the upward-propagating migrating diurnal tide above 96 km. Instead, our results suggest that the mean meridional circulation induced by dissipating tides plays a major role in tidal mixing.

[44] As has been demonstrated, upward-propagating tides influence daytime F region plasma density at low latitudes through both electrodynamic effects and tidal mixing

effects. It is thus necessary to be cautious when observations are interpreted. For example, low-latitude *F* region plasma density is greatest during equinoctial months [e.g., *Millward et al.*, 1996; *Burns et al.*, 2012]. This is sometimes considered as the result of an enhanced equatorial plasma fountain due to strong upward-propagating tides [e.g., *Ma et al.*, 2003]. As a matter of fact, the upward-propagating migrating diurnal tide is largest in amplitude during the equinoxes [*Burrage et al.*, 1995; *McLandress*, 2002], and similar equinoctial maxima can be found in J_{total} and V_z [e.g., *Yamazaki et al.*, 2011; *Fejer et al.*, 2008]. According to our simulation results, however, strong upward-propagating tides cause an enhancement of tidal mixing that reduces the *F* region plasma density on a seasonal time scale. Indeed, when the TIE-GCM is run continuously for a year with and without lower-boundary tidal forcing, the nonforcing run provides a larger seasonal variation in the ionospheric plasma density, as recently shown by *Chang et al.* [2013]. Therefore, the high plasma density during the equinoxes is not necessarily related to the seasonal variation of upward-propagating tides. It is more likely due to other mechanisms that bring about a high $[O_1]/[N_2]$ ratio during the equinoxes. *Fuller-Rowell* [1998] showed that, during the equinoxes, the interhemispheric circulation is much less than during the solstices, because the difference in solar heating between the two hemispheres is small, and this makes the thermosphere less mixed during the equinoxes than solstices, leading to a relatively higher $[O_1]/[N_2]$ ratio during the equinoxes. He called this mechanism the "thermospheric spoon" on the analogy between a tea spoon stirring fluid and the global-scale wind mixing the thermosphere. An additional mechanism was recently proposed by *Qian et al.* [2009, 2013], in which seasonal thermospheric composition changes and associated ionospheric changes are attributed to seasonally varying eddy diffusivity induced by gravity waves. Their results suggest that reduced eddy diffusivity in the MLT region during the equinoxes causes a high $[O_1]/[N_2]$ ratio in the whole thermosphere. The relative importance of tidal mixing, thermospheric spoon, and gravity wave-induced turbulence in the generation of ionospheric seasonal variations needs to be evaluated in the future.

[45] The present study considered effects only of migrating upward-propagating tides. In the MLT region, nonmigrating tides are comparable in amplitude to migrating tides [e.g., *Forbes et al.*, 2008], and thus nonmigrating tides could also produce significant effects on the ionosphere. In fact, observational and numerical studies have shown that upward-propagating nonmigrating tides play an essential role in producing a longitudinal structure in *F* region plasma density [e.g., *Immel et al.*, 2006; *Hagan et al.*, 2007] and thermospheric neutral density [e.g., *Kwak et al.*, 2012; *Wan et al.*, 2012]. A numerical study by *Angelats i Coll and Forbes* [2002] showed that the zonal-mean winds induced by westward-propagating semidiurnal nonmigrating tides tend to reinforce those induced by migrating tides. Eastward propagating tides like the DE3 (diurnal eastward wave number 3) may be expected to induce mean zonal winds that are eastward. The relative importance of nonmigrating tides in producing electrodynamic effects and tidal mixing effects on the ionosphere needs to be studied. Also, the dependence of the tidal effects on season and solar activity needs to be examined. Equatorial *F* region plasma drift measurements have shown that the day-to-day variability increases with decreasing solar activity [*Fejer and Scherliess*, 2001]. A numerical study by *Liu and Richmond* [2013] showed that the contribution of variable tides from the lower atmosphere to ionospheric variability is more significant for lower solar activity conditions, when the relative contribution of thermospherically generated tides to the ionospheric wind dynamo is weaker.

[46] Finally, observational studies to verify our theoretical predictions are encouraged. There exists some evidence supportive of electrodynamical effects on the ionosphere through upward-propagating tides. For example, recent studies have revealed that upward-propagating tides in the MLT region are significantly influenced by a stratospheric sudden warming (SSW) [e.g., *Sridharan et al.*, 2009]. An SSW can disrupt the global circulation in the middle atmosphere. Thus, it affects the propagation characteristics of the tides from the troposphere and stratosphere, which modulates the amplitude and phase of the tides in the MLT region [*Stening et al.*, 1997; *Fuller-Rowell et al.*, 2010; *Pedatella et al.*, 2012]. Ionospheric observations during SSW events have revealed consistent tidal signatures in electric currents, equatorial electric fields, and low-latitude electron density [*Yamazaki et al.*, 2012b; *Fejer et al.*, 2010; *Goncharenko et al.*, 2010], clearly demonstrating an electrodynamical coupling due to upward-propagating tides. On the other hand, observational evidence for tidal mixing effects on the ionosphere are few. The slow response of the ionosphere to tidal mixing (see Figure 3) makes it difficult to isolate the effects from the variability related to geomagnetic activity. Since both the ionosphere and thermosphere are sensitive to geomagnetic activity, data for extremely quiet magnetic conditions will be necessary for the analysis.

[47] **Acknowledgments.** We are grateful to Hanli Liu for his helpful comments on earlier drafts. We are also grateful to Astrid Maute for her assistance in the simulations. Y.Y. was supported by a Research Fellowship of the Japan Society for the Promotion of Science (JSPS) for Research Abroad. The National Center for Atmospheric Research is sponsored by the National Science Foundation.

[48] Robert Lysak thanks the reviewers for their assistance in evaluating this paper.

References

Akmaev, R. A., and G. M. Shved (1980), Modeling of the composition of the lower thermosphere taking into account of the dynamics with applications to tidal variations of the [OI] 5577Åairglow, *J. Atmos. Terr. Phys.*, *42*, 705–716.

Angelats i Coll, M., and J. M. Forbes (2002), Nonlinear interactions in the upper atmosphere: The s = 1 and s = 3 nonmigrating semidiurnal tides, *J. Geophys. Res.*, *107*(A8), 1157, doi:10.1029/2001JA900179.

Balan, N., and K. N. Iyer (1983), Equatorial anomaly in ionospheric electron content and its relation to dynamo currents, *J. Geophys. Res.*, *88* (A12), 10,259–10,262, doi:10.1029/JA088iA12p10259.

Burns, A. G., S. C. Solomon, W. Wang, L. Qian, Y. Zhang, and L. J. Paxton (2012), Daytime climatology of ionospheric N_mF_2 and h_mF_2 from COSMIC data, *J. Geophys. Res.*, *117*, A09315, doi:10.1029/2012JA017529.

Burrage, M. D., M. E. Hagan, W. R. Skinner, D. L. Wu, and P. B. Hays (1995), Long-term variability in the solar diurnal tide observed by HRDI and simulated by the GSWM, *Geophys. Res. Lett.*, *22*, 2641–2644.

Chang, L. C., S. E. Palo, and H.-L. Liu (2011), Short-term variability in the migrating diurnal tide caused by interactions with the quasi 2 day wave, *J. Geophys. Res.*, *116*, D12112, doi:10.1029/2010JD014996.

Chang, L. C., C.-H. Lin, J.-Y. Liu, N. Balan, J. Yue, and J.-T. Lin (2013), Seasonal and local time variation of ionospheric migrating tides in 2007–2011 FORMOSAT-3/COSMIC and TIE-GCM total electron content, *J. Geophys. Res. Space Physics*, *118*, 2545–2564, doi:10.1002/jgra.50268.

Chapman, S., and J. Bartels (1940), *Geomagnetism*, Oxford Univ. Press, London, U.K.

Chen, C. H., J. Y. Liu, K. Yumoto, C. H. Lin, and T. W. Fang (2008), Equatorial ionization anomaly of total electron content and equatorial electrojet in ground-based geomagnetic field strength, *J. Atmos. Sol. Terr. Phys.*, *70*, 2172–2183, doi:10.1016/j.jastp.2008.09.021.

Colegrove, F. D., F. S. Johnson, and W. B. Hanson (1966), Atmospheric composition in the lower thermosphere, *J. Geophys. Res.*, *71*(9), 2227–2236, doi:10.1029/JZ071i009p02227.

Dickinson, R. E., E. C. Ridley, and R. G. Roble (1981), A three-dimensional general circulation model of the thermosphere, *J. Geophys. Res.*, *86*, 1499–1512.

Dickinson, R. E., E. C. Ridley, and R. G. Roble (1984), Thermospheric general circulation with coupled dynamics and composition, *J. Atmos. Sci.*, *41*, 205–219.

Fang, T. W., A. D. Richmond, J. Y. Liu, A. Maute, C. H. Lin, C. H. Chen, and B. Harper (2008), Model simulation of the equatorial electrojet in the Peruvian and Philippine sectors, *J. Atmos. Sol. Terr. Phys.*, *70*, 2203–2211.

Fejer, B. G., and Scherliess (2001), On the variability of equatorial F-region vertical plasma drifts, *J. Atmos. Sol. Terr. Phys.*, *63*, 893–897.

Fejer, B. G., J. W. Jensen, and S.-Y. Su (2008), Quiet time equatorial F region vertical plasma drift model derived from ROCSAT-1 observations, *J. Geophys. Res.*, *113*, A05304, doi:10.1029/2007JA012801.

Fejer, B. G., M. E. Olson, J. L. Chau, C. Stolle, H. Lühr, L. P. Goncharenko, K. Yumoto, and T. Nagatsuma (2010), Lunar-dependent equatorial ionospheric electrodynamic effects during sudden stratospheric warmings, *J. Geophys. Res.*, *115*, A00G03, doi:10.1029/2010JA015273.

Fesen, C. G., G. Crowley, R. G. Roble, A. D. Richmond, and B. G. Fejer (2000), Simulation of the pre-reversal enhancement in the low latitude vertical ion drifts, *Geophys. Res. Lett.*, *13*, 1851–1854, doi:10.1029/2000GL000061.

Fesen, C. G., D. L. Hysell, J. M. Meriwether, M. Mendillo, B. G. Fejer, R. G. Roble, B. W. Reinisch, and M. A. Biondi (2002), Modeling the low-latitude thermosphere and ionosphere, *J. Atmos. Sol. Terr. Phys.*, *64*, 1337–1349.

Forbes, J. M. (1984), Middle atmosphere tides, *J. Atmos. Terr. Phys.*, *46*, 1049–1067.

Forbes, J. M., R. G. Roble, and C. G. Fesen (1993), Acceleration, heating, and compositional mixing of the thermosphere due to upward propagating tides, *J. Geophys. Res.*, *98*(A1), 311–321.

Forbes, J. M., X. Zhang, S. Palo, J. Russell, C. J. Mertens, and M. Mlynczak (2008), Tidal variability in the ionospheric dynamo region, *J. Geophys. Res.*, *113*, A02310, doi:10.1029/2007JA012737.

Fuller-Rowell, T. J. (1998), The thermospheric spoon: A mechanism for the semiannual density variation, *J. Geophys. Res.*, *103*(A3), 3951–3956, doi:10.1029/97JA03335.

Fuller-Rowell, T., F. Wu, R. Akmaev, T.-W. Fang, and E. Araujo-Pradere (2010), A whole atmosphere model simulation of the impact of a sudden stratospheric warming on thermosphere dynamics and electrodynamics, *J. Geophys. Res.*, *115*, A00G08, doi:10.1029/2010JA015524.

Goncharenko, L. P., A. J. Coster, J. L. Chau, and C. E. Valladares (2010), Impact of sudden stratospheric warmings on equatorial ionization anomaly, *J. Geophys. Res.*, *115*, A00G07, doi:10.1029/2010JA015400.

Goncharenko, L. P., A. J. Coster, R. A. Plumb, and D. I. V. Domeisen (2012), The potential role of stratospheric ozone in the stratosphere-ionosphere coupling during stratospheric warmings, *Geophys. Res. Lett.*, *39*, L08101, doi:10.1029/2012GL051261.

Hagan, M. E., R. G. Roble, and J. Hackney (2001), Migrating thermospheric tides, *J. Geophys. Res.*, *106*(A7), 12739–12752, doi:10.1029/2000JA000344.

Hagan, M. E., and J. M. Forbes (2002), Migrating and nonmigrating diurnal tides in the middle and upper atmosphere excited by tropospheric latent heat release, *J. Geophys. Res.*, *107*(D24), 4754, doi:10.1029/2001JD001236.

Hagan, M. E., and J. M. Forbes (2003), Migrating and nonmigrating semidiurnal tides in the upper atmosphere excited by tropospheric latent heat release, *J. Geophys. Res.*, *108*(A2), 1062, doi:10.1029/2002JA009466.

Hagan, M. E., A. Maute, R. G. Roble, A. D. Richmond, T. J. Immel, and S. L. England (2007), Connections between deep tropical clouds and the Earth's ionosphere, *Geophys. Res. Lett.*, *34*, L20109, doi:10.1029/2007GL030142.

Hanson, W. B., and R. J. Moffett (1966), Ionization transport effects in the equatorial *F*-region, *J. Geophys. Res.*, *71*, 5559–5572.

Heelis, R. A., J. K. Lowell, and R. W. Spiro (1982), A model of the high-latitude ionospheric convection pattern, *J. Geophys. Res.*, *87*, 6339–6345.

Immel, T. J., E. Sagawa, S. L. England, S. B. Henderson, M. E. Hagan, S. B. Mende, H. U. Frey, C. M. Swenson, and L. J. Paxton (2006), Control of equatorial ionospheric morphology by atmospheric tides, *Geophys. Res. Lett.*, *33*, L15108, doi:10.1029/2006GL026161.

Jee, G., R. W. Schunk, and L. Scherliess (2004), Analysis of TEC data from the TOPEX/Poseidon mission, *J. Geophys. Res.*, *109*, A01301, doi:10.1029/2003JA010058.

Khattatov, B. V., V. A. Yubin, M. A. Geller, P. B. Hays, and R. A. Vincent (1997a), Diurnal migrating tide as seen by the high-resolution Doppler imager/UARS: 1. Monthly mean global meridional winds, *J. Geophys. Res.*, *102*(D4), 4405–4422, doi:10.1029/96JD03655.

Khattatov, B. V., M. A. Geller, V. A. Yubin, and P. B. Hays (1997b), Diurnal migrating tide as seen by the high-resolution Doppler imager/UARS: 2. Monthly mean global zonal and vertical velocities, pressure, temperature, and inferred dissipation, *J. Geophys. Res.*, *102*(D4), 4423–4435, doi:10.1029/96JD03654.

Kwak, Y.-S., H. Kil, W. K. Lee, S.-J. Oh, and Z. Ren (2012), Nonmigrating tidal characteristics in thermospheric neutral mass density, *J. Geophys. Res.*, *117*, A02312, doi:10.1029/2011JA016932.

Lindzen, R. S., and S. Chapman (1969), Atmospheric tides, *Space Sci. Rev.*, *10*, 3–188.

Liu, H.-L., W. Wang, A. D. Richmond, and R. G. Roble (2010), Ionospheric variability due to planetary waves and tides for solar minimum conditions, *J. Geophys. Res.*, *115*, A00G01, doi:10.1029/2009JA015188.

Liu, H.-L., and A. D. Richmond (2013), Attribution of ionospheric vertical plasma drift perturbations to large-scale waves and the dependence on solar activity, *J. Geophys. Res. Space Physics*, *118*, 2452–2465, doi:10.1002/jgra.50265.

Ma, R., J. Xu, and H. Liao (2003), The features and a possible mechanism of semiannual variation in the peak electron density of the low latitude F2 layer, *J. Atmos. Sol. Terr. Phys.*, *65*, 47–57.

McLandress, C., G. G. Shepherd, B. H. Solheim, M. D. Burrage, P. B. Hays, and W. R. Skinner (1996), Combined mesosphere/thermosphere winds using WINDII and HRDI data from the Upper Atmosphere Research Satellite, *J. Geophys. Res.*, *101*(D6), 10,441–10,453, doi:10.1029/95JD01706.

McLandress, C. (2002), The seasonal variation of the propagating diurnal tide in the mesosphere and lower thermosphere. Part II: The role of tidal heating and zonal mean zonal winds, *J. Atmos. Sci.*, *59*, 907–921.

Millward, G. H., H. Rishbeth, T. J. Fuller-Rowell, A. D. Aylward, S. Quegan, and R. J. Moffett (1996), Ionospheric F_2 layer seasonal and semiannual variations, *J. Geophys. Res.*, *101*(A3), 5149–5156, doi:10.1029/95JA03343.

Millward, G. H., I. C. F. Müller-Wodarg, A. D. Aylward, T. J. Fuller-Rowell, A. D. Richmond, and R. J. Moffett (2001), An investigation into the influence of tidal forcing on F region equatorial vertical ion drift using a global ionosphere-thermosphere model with coupled electrodynamics, *J. Geophys. Res.*, *106*(A11), 24,733–24,744, doi:10.1029/2000JA000342.

Miyahara, S. (1978), Zonal mean wind induced by vertically propagating atmospheric tidal waves in the lower thermosphere, *J. Meteor. Soc. Japan*, *56*, 86–97.

Miyahara, S., and D. H. Wu (1989), Effects of solar tides on the zonal mean circulation in the lower thermosphere: Solstice condition, *J. Atmos. Terr. Phys.*, *51*, 635–648.

Müller-Wodarg, I. C. F., and A. D. Aylward (1998), The influence of tides on composition of the thermosphere, *Adv. Space Res.*, *21*, 807–810.

Pedatella, N. M., H.-L. Liu, A. D. Richmond, A. Maute, and T.-W. Fang (2012), Simulations of solar and lunar tidal variability in the mesosphere and lower thermosphere during sudden stratosphere warmings and their influence on the low-latitude ionosphere, *J. Geophys. Res.*, *117*, A08326, doi:10.1029/2012JA017858.

Qian, L., S. C. Solomon, and T. J. Kane (2009), Seasonal variation of thermospheric density and composition, *J. Geophys. Res.*, *114*, A01312, doi:10.1029/2008JA013643.

Qian, L., A. G. Burns, S. C. Solomon, and W. Wang (2013), Annual/semiannual variation of the ionosphere, *Geophys. Res. Lett.*, *40*, 1928–1933, doi:10.1002/grl.50448.

Rastogi, R. G., and J. A. Klobuchar (1990), Ionospheric electron content within the equatorial F_2 layer anomaly belt, *J. Geophys. Res.*, *95*(A11), 19,045–19,052, doi:10.1029/JA095iA11p19045.

Richards, P. G., J. A. Fennelley, and D. G. Torr (1994), EUVAC: A solar EUV Flux Model for aeronomic calculations, *J. Geophys. Res.*, *99*(A5), 8981–8992, doi:10.1029/94JA00518.

Richmond, A. D. (1979), Ionospheric wind dynamo theory: A review, *J. Geomag. Geoelectr.*, *31*, 287–310.

Richmond, A. D. (1989), Modeling the ionosphere wind dynamo: A review, *Pure Appl. Geophys.*, *47*, 413–435.

Richmond, A. D. (1995), Ionospheric electrodynamics using magnetic apex coordinates, *J. Geomagn. Geoelectr.*, *47*, 191–212.

Richmond, A. D., and R. G. Roble (1987), Electrodynamic effects of the thermospheric winds from the NCAR thermospheric general circulation model, *J. Geophys. Res.*, *92*(A11), 12,365–12,376.

Richmond, A. D., E. C. Ridley, and R. G. Roble (1992), A thermosphere/ionosphere general circulation model with coupled electrodynamics, *Geophys. Res. Lett.*, *19*(6), 601–604, doi:10.1029/92GL00401.

Roble, R. G. (1995), Energetics of the mesosphere and thermosphere, in *The Upper Mesosphere and Lower Thermosphere: A Review of Experiment and Theory, Geophys. Monogr. Ser.,* vol. 87, edited by R. M. Johnson and T. L. Killeen, pp. 1–21, AGU, Washington, D. C., doi:10.1029/GM087p0001.

Roble, R. G., and E. C. Ridley (1994), A thermosphere-ionosphere-mesosphere-electrodynamics general-circulation model (time-GCM): Equinox solar cycle minimum simulations (30–500 km), *Geophys. Res. Lett.*, *21*, 417–420.

Roble, R. G., E. C. Ridley, A. D. Richmond, and R. E. Dickinson (1988), A coupled thermosphere/ionosphere general circulation model, *Geophys. Res. Lett.*, *15*, 1325–1328.

Solomon, S. (2006), Numerical models of the E-region ionosphere, *Adv. Space Res.*, *37*, 1031–1037.

Sridharan, S., S. Sathishkumar, and S. Gurubaran (2009), Variabilities of mesospheric tides and equatorial electrojet strength during major stratospheric warming events, *Ann. Geophys.*, *27*, 4125–4130, doi:10.5194/angeo-27-4125-2009.

Stening, R. J., J. M. Forbes, M. E. Hagan, and A. D. Richmond (1997), Experiments with a lunar atmospheric tidal model, *J. Geophys. Res.*, *102*(D12), 13,465–13,471, doi:10.1029/97JD00778.

Swinbank, R., and D. A. Ortland (2003), Compilation of wind data for the Upper Atmosphere Research Satellite (UARS) reference atmosphere project, *J. Geophys. Res.*, *108*(D19), 4615, doi:10.1029/2002JD003135.

Takeda, M. (2002), Features of global geomagnetic S_q field from 1980 to 1990, *J. Geophys. Res.*, *107*(A9), 1252, doi:10.1029/2001JA009210.

Vial, F., J. M. Forbes, and S. Miyahara (1991), Some transient aspects of tidal propagation, *J. Geophys. Res.*, *96*(A2), 1215–1224, doi:10.1029/90JA02181.

Wan, W., Z. Ren, F. Ding, J. Xiong, L. Liu, B. Ning, B. Zhao, G. Li, and M.-L. Zhang (2012), A simulation study for the couplings between DE3 tide and longitudinal WN4 structure in the thermosphere and ionosphere, *J. Atmos. Sol. Terr. Phys.*, *90-91*, 52–60, doi:10.1016/j.jastp.2012.04.011.

Watanabe, S., S. Miyahara, and Y. Miyoshi (1999), Lagrangian transport experiments in the MLT region, *Earth Planets Space*, *51*, 745–750.

Wu, Q., T. L. Killeen, D. A. Ortland, S. C. Solomon, R. D. Gablehouse, R. M. Johnson, W. R. Skinner, R. J. Niciejewski, and S. J. Franke (2006), TIMED Doppler Interferometer (TIDI) observations of migrating diurnal and semi-diurnal tides, *J. Atmos. Sol. Terr. Phys.*, *68*, 408–417, doi:10.1016/j.jastp.2005.02.031.

Yamazaki, Y., et al. (2011), An empirical model of the quiet daily geomagnetic field variation, *J. Geophys. Res.*, *116*, A10312, doi:10.1029/2011JA016487.

Yamazaki, Y., A. D. Richmond, H. Liu, K. Yumoto, and Y. Tanaka (2012a), Sq current system during stratospheric sudden warming events in 2006 and 2009, *J. Geophys. Res.*, *117*, A12313, doi:10.1029/2012JA018116.

Yamazaki, Y., K. Yumoto, D. McNamara, T. Hirooka, T. Uozumi, K. Kitamura, S. Abe, and A. Ikeda (2012b), Ionospheric current system during sudden stratospheric warming events, *J. Geophys. Res.*, *117*, A03334, doi:10.1029/2011JA017453.

Yoshikawa, M., and S. Miyahara (2003), Zonal mean meridional circulation in the low to middle latitude of MLT region: A numerical simulation by a general circulation model, *Adv. Space Res.*, *32*(5), 709–717.

Zhang, S. P., C. McLandress, and G. G. Shepherd (2007), Satellite observations of mean winds and tides in the lower thermosphere: 2. Wind Imaging Interferometer monthly winds for 1992 and 1993, *J. Geophys. Res.*, *112*, D21105, doi:10.1029/2007JD008457.